

Tea Polyphenol Modified, Photothermal Responsive and ROS Generative Black Phosphorus Quantum Dots as Nanoplatfoms for Promoting MRSA Infected Wounds Healing in Diabetic Rats

Shibo Xu

Jinzhou Medical University

Linna Chang

Jinzhou Medical University

Xingjun Zhao

Jinzhou Medical University

Yanan Hu

Jinzhou Medical University

Shuocheng Huang

Jinzhou Medical University

Zhenhua Chen (✉ zhchen561@yahoo.com)

Jinzhou Medical University <https://orcid.org/0000-0002-0161-0236>

Xiuli Ren

Jinzhou Medical University

Xifan Mei

Jinzhou Medical University

Research Article

Keywords: multifunctional nanoplatfoms, black phosphorus quantum dots, diabetic deep-burn wound healing, photocatalytic, photothermal

Posted Date: September 15th, 2021

DOI: <https://doi.org/10.21203/rs.3.rs-871716/v1>

License:   This work is licensed under a Creative Commons Attribution 4.0 International License.

[Read Full License](#)

Version of Record: A version of this preprint was published at Journal of Nanobiotechnology on November 10th, 2021. See the published version at <https://doi.org/10.1186/s12951-021-01106-w>.

Abstract

Background

Healing of MRSA (methicillin-resistant *Staphylococcus aureus*) infected deep burn wounds (MIDBW) in diabetic patients remains an obstacle, but is a cutting-edge research problem in clinical science. Surgical debridement and continuous antibiotic use remain the primary clinical treatment for MIDBW. However, suboptimal pharmacokinetics and high doses of antibiotics often cause serious side effects such as fatal complications of drug-resistant bacterial infections. MRSA, which causes wound infection, is currently a bacterium of concern in the treatment of diabetic wound healing, and in more severe cases it can even lead to amputation of the patient's limb.

Results

The present work proposed a strategy of using EGCG (Epigallocatechin gallate) modified black phosphorus quantum dots (BPQDs) as a therapeutic nanoplatform for MIDBW to achieve the synergistic functions of NIR (near infrared)-response, ROS-generation, sterilization and promoted wound healing. The electron spin resonance results revealed that EGCG-BPQDs@H had a stronger photocatalytic ability to produce singlet oxygen than BPQDs@H and the inhibition results indicated an effective bactericidal rate of 88.6% against MRSA. Molecular biology analysis demonstrated that EGCG-BPQDs significantly upregulated CD31 nearly 4-fold and basic fibroblast growth factor (bFGF) nearly 2-fold, which were beneficial for promoting proliferation of vascular endothelial cells and skin epidermal cells. Under NIR irradiation, EGCG-BPQDs hydrogel (EGCG-BPQDs@H) treated MIDBW area could rapidly raise temperature up to 55°C for sterilization. The MIDBW closure rate of rat after 21 days of treatment was 92.4%, much better than that of 61.1% of the control group. The engineered EGCG-BPQDs@H were found to promote MIDBW healing by triggering the PI3K/AKT and ERK1/2 signaling pathways, which could enhance cell proliferation and differentiation. In addition, intravenous circulation experiment showed good biocompatibility of EGCG-BPQDs@H, no obvious damage to rat major organs were observed.

Conclusions

The obtained results demonstrated that EGCG-BPQDs@H achieved the synergistic functions of photocatalytic property, photothermal effects and promoted wound healing, and are promising multifunctional nanoplatforms for MIDBW healing in diabetics.

1. Introduction

MRSA infected deep-burn wound in diabetic patients is a fatal threat to human health and the frontier in clinical medicine [1]. Surgical debridement and continuous use of antibiotics are still the main clinical treatment for MIDBW [2, 3]. However, suboptimal pharmacokinetics, and large doses of antibiotics usually caused severe side effects, like deadly complications of resistant bacteria infection [4]. MRSA, which causes wound infections, is currently a bacteria of concern in the treatment of diabetic wound healing,

and in more severe cases, it can even cause amputation of the patient's limb [5, 6]. The even worse, the development of new antibiotics has not been realized for a long time worldwide [7]. Therefore, besides surgical debridement and continuous use of antibiotics, multifunctional collaborative therapy nanoplatform is much attracting for MIDBW in in diabetic patients. To date, various nanomaterials have been currently available in diabetic infected wound healing, such as metal-organic frameworks [8, 9], dopamine [10–13], peptides [14], metal oxides and nano silver [15, 16]. These excellent pioneered works suggest that multifunctional nanoplatforms with advantages of both strong antibacterial and effective promoting of wound healing function are attractive, promising strategy for the treatment of infected wound.

Among these numerous antibacterial materials, black phosphorus (BP) is attracting because of its broad optical absorption and striking charge carrier mobility, exhibiting outstanding singlet oxygen (1O_2) activation and high temperature generation under NIR irradiation [17,18]. Recently, photocatalytic properties and photothermal activity have been intensively investigated in biomedical application [19], especially in the field of anti-infection wound treatments by their virtues of minimally invasive, effectively sterilization and easily operation [20–22]. These reported excellent works disclosed the attracting prospect of BP in infected wound healing. However, these documents mostly focused on BP nanosheets, while BPQDs have seldomly been researched, particularly in MIDBW. Therefore, construction of multifunctional BPQDs nanoplatform with collaborative properties of NIR response, ROS generation, sterilization and promoted wound healing, is a challengeable but much attracting strategy for MIDBW therapy.

Herein, in order to achieve multifunctional BPQDs nanoplatform, we proposed a strategy of constructing EGCG-modified BPQDs. As illustrated in Scheme 1, firstly, EGCG molecules were modified on BPQDs by the virtue of the interactions between -OH group on EGCG and P atoms from BPQDs, such as hydrogen bond and molecule interactions. Our previous works have proved the functions of these kinds of interactions among EGCG and other building blocks in forming nanohydrogels and the excellent biological function in promoting wound recovery of EGCG [23, 24]. Then, the obtained EGCG-BPQDs were loaded into hydrogels as a dual-purpose nano-agent to possess antibacterial effect and accelerate wound healing effect simultaneously. Specifically, the engineered nanomaterials are expected to promote angiogenesis and epithelial regeneration by upregulating cellular CD31 and bFGF expression. Furthermore, under NIR irradiation, the nanomaterials will induce high levels of ROS production to eradicate the antibiotic-resistant bacterial infections, while generating local heat and accelerating microcirculatory blood flow. Our previous work and related reported woks have explored hydrogels can be used as excellent drug delivery systems [25]. Hydrogels encapsulated with EGCG-BPQDs will provide sustainable moisture and long release of EGCG-BPQDs, which are benefit for wound healing. Finally, the constructed hydrogels encapsulated EGCG-BPQDs are expected to achieve functional properties of antibacterial, vascular regeneration and accelerated epithelial regeneration.

2. Materials And Methods

2.1 Materials

Methicillin-resistant *Staphylococcus aureus* (MRSA) and Gram-negative bacteria *Escherichia coli* (*E. coli*) were purchased from Guangdong Microbial Culture Collection (China). Dulbecco's modified Eagle's medium (DMEM), 3-(4,5-Dimethylthiazol-2-yl)-2,5-diphenyl tetrazolium bromide (MTT), and fetal bovine serum (FBS) were purchased from Gibco (USA). Human skin keratinocytes cells (HaCat) and human umbilical vein endothelial cells (HUVEC) were obtained from American type culture collection (ATCC). The 2,2'-bis(anthracene-9,10-diylbis(methylene))-dimalonic acid (ABDA) was supplied from Shanghai Civi Chemical Technology Co., Ltd. 1-methyl-2-pyrrolidone (NMP) was purchased from Aladdin. The primary antibodies to CD31, VEGF, bFGF, Tubulin were obtained from Cell Signaling Technology (USA). We used deionized water through the experiment.

2.2 Characterization

The component of EGCG-BPQD@H was identified by Fourier transform infrared spectroscopy (FTIR, SHIMADZU, Kyoto, Japan) with the KBr disk method. Relevant fluorescence data were acquired with a fluorescence photometer (F97PRO, Shanghai, China). UV-vis data were measured by UV-vis spectrophotometer (PerkinElmer Lambda 605S UV-vis spectrometer) at room temperature. The sample's crystal structure was tested by X-ray diffraction (XRD, Shimadzu, Kyoto, Japan) and Cu K radiation. We also used dynamic laser scattering (DLS, Malvern, Nano ZS90, Worcestershire, UK) to test the sample's particle size. The sample's appearance characteristics were displayed through a transmission electron microscope (TEM, JEM-1200EX, Tokyo, Japan). Infrared thermal imager and NIR laser were purchased from Dongguan Bufan Electronics Co., Ltd., China. Confocal laser scanning microscopy (CLSM, Leica TSCSP5 confocal unit) was used to observe the expression of related proteins in cells.

2.3 Therapy of burn wounds infected with MRSA in diabetic rats

All animal experiments were carried out according to the Guidelines for Care and Use of Laboratory Animals of Jinzhou Medical University. Male Sprague-Dawley rats, having the weight of 190 ± 20 g, were obtained from Vital River Company (Beijing, China). After one week of acclimatization at the animal holding unit, the rats were ready for next experiments. Diabetic animal model was established with streptozotocin (STZ; St. Louis Sigma, Missouri; 80 mg/kg) and rats were injected intraperitoneally with STZ (0.1 M pH 4.5 citrate buffer formulation) once daily for four days. Rats with blood glucose levels greater than 300 mg/dL were selected for the test. Briefly, the dorsal hair was shaved and decontaminated after anesthetization, and then the electric device heated at 120°C was contact with the shaved dorsal skin for 12 sec to cause a diameter of ~ 13 mm deep partial-thickness burn injury. Then the burn area was injected 100 μ L of MRSA suspension were diluted to 2.0×10^7 CFU/mL to build an experimental model of infection. After continuous infection for 3 days, the prepared hydrogel, BPQDs@H, EGCG@H and EGCG-BPQDS@H were applied to the wound once daily directly. Meanwhile, the infected wound area was photographed at the same height and the size of wounds were measures by vernier caliper. The control + NIR, BPQDs@H + NIR, EGCG@H + NIR and EGCG-BPQDS@H + NIR groups were

treated with 808 nm laser (2.5 W/cm^2 , 5 min), and the temperature changes of wounds were monitored via thermographic pictures captured by infrared thermal imaging system. Then body weight of rats was registered every time. The burn wounds tissues and systemic organs were harvested for protein extraction and histological analyses etc.

2.4. In vitro antibacterial activity analyses

After activation and incubation, MRSA and *E. coli* were cultured at 37°C in fresh liquid LB medium. Briefly, the MRSA and *E. coli* ($1.0 \times 10^8 \text{ CFU/mL}$) were extended into the LB-Agar-Medium. After that, filter papers containing EGCG-BPQDs@H or other nanomaterials were spread on the MRSA and *E. coli* agar plates as a method of antibacterial activity evaluation. Each group's diameters of the bacteriostatic ring were measured after incubation for 24 h. We also used the MRSA and *E. coli* to estimate the synergetic antibacterial effects of EGCG-BPQDs@H plus NIR laser irradiation. Logarithmic growth phase bacteria were incubated in LB medium and then mixed with each group of materials in a 1.5 mL Solarbio tube containing $100\mu\text{L}$ of normal saline. For all groups, the bacteria were illuminated with/without NIR laser (808 nm , 2.5 W/cm^2) for 10 min and were incubated for another 24 h in the LB-Agar-Medium for CFU. In addition, to observe the antibacterial effect of different groups directly, bacterial morphology was examined by scanning electron microscope (SEM).

2.5 Calcein-AM/PI staining

The antibacterial effect was measured by double fluorescent dye method. Specifically, bacteria were treated with hydrogel, BPQDs@H, EGCG@H, or EGCG-BPQDs@H for 3 hours at 37°C . For all groups, the bacteria were irradiated with/without NIR laser (2.5 W/cm^2 , 10 min). Bacteria were incubated with calcein-AM and PI (Solarbio, China) after centrifuging at 5000 rpm for 5min. Then, the bacteria were washed with phosphate-buffered saline (PBS), and placed on glass slides. The bacteria with different treatments were presented under fluorescence microscope (Leica DM4000B, Germany). The red fluorescent nucleic acid dye PI, which can penetrate the damaged cell wall, was used to mark dead bacteria. On the contrast, the Calcein-AM that penetrated the living cell membrane was cleaved by the intracellular esterase to form Calcein, which emitted strong green fluorescence and remained in the live bacteria.

2.6 Photocatalytic property of EGCG-BPQDs@H

The ABDA probes were applied to detect singlet oxygen generation and time-varying changes. The fluctuation of ABDA probes was recorded to reflect the generation of ROS. We added EGCG-BPQDs@H into the 5mM ABDA solution and then irradiated it under near-infrared laser. The test was performed every 5min. In addition, the single linear state of oxygen produced is detected by electron spin resonance spectroscopy.

The intracellular ROS level of bacteria was measured by fluorescent probe, 2',7'-dichlorodihydrofluorescein diacetate (DCFH-DA, Beyotime, China), which could be deacetylated and oxidized to fluorescent products. The MRSA after various treatments were fixed with 4% paraformaldehyde, and then incubated with DCFH-DA probe for 30 min in the dark. The fluorescence

imaging was immediately recorded with Leica DM4000B microscope. The fluorescent intensity was measured via ImageJ and Fiji12 plugin to quantify the total ROS level via EGCG-BPQDs@H.

2.7 Determination of protein leakage

The leakage of protein through the membrane of MRSA was observed after exposing different samples. NIR-treated groups were irradiated with 808 nm NIR light for 20 min at a power density of 2.5 W/cm². Subsequently, the bacterial suspension supernatant was collected by centrifugation at 12000 rpm for 5 min. Finally, the supernatant liquid was immediately withdrawn and seeded into a 96-well plate. The protein intensities of different groups was determined by the microplate reader at 562 nm through the BCA assay kit (Beyotime, China) to determine the relative protein leakage of each sample.

2.8 Biofilm formation assay

MRSA biofilm model was employed to assess the antibiofilm ability of EGCG-BPQDs@H antibacterial nanoplateforms. 2 mL of 5×10^8 CFU mL⁻¹ of MRSA was seeded into a 24-well plate and incubated 48 hours to establish biofilm. After different treatments, crystal violet (CV) staining was utilized to evaluate the antibiofilm effect. MRSA biofilms were washed with gentle running deionized water to remove the unbound dye. The bound CV was dissolved using absolute ethanol. At last, a microplate reader was used to measure the absorbance of all samples at 590 nm.

2.9 Histology analyses

In the infected burn wound healing experiment, individual wound tissues and major organs of the rats were harvested for histological analysis. The tissues were fixed in 4% formaldehyde and dehydrated through alcohol. The paraffin embedded tissues were cut to a 5µm thickness and were stained with hematoxylin and eosin (H&E) and Masson stain to evaluate the recovery of wound healing. Besides, the biocompatibility of nanomaterials in vivo is assessed by H&E staining of main organs. The sections were captured with Leica DM4000B microscope.

2.10 In vitro angiogenesis assay of HUVECs

The angiogenesis ability of EGCG-BPQDs@H in vitro was assessed by endothelial tube-like formation as specified by the manufacturer's guidelines. HUVEC were used for this assay. The night before the experiment, pipette tips and well plates were placed in a -20°C freezer and the Matrigel (BD Biosciences, USA) thawed at 4°C. First, 80µL Matrigel was incubated into 96-well plate for 30 min at 37°C to induce gelation. 1.0×10^4 HUVECs were first seeded on EGCG-BPQDS@H or BPQDs@H or EGCG@H with 100µL of FBS-free culture medium above solidified Matrigel for 6h. finally, the differentiations of HUVECs were observed through an inverted phase contrast microscope (Leica DM4000B, Germany). The total length and number of nodes and segments were digitally imaged and quantified using the Angiogenesis Analyzer macro in ImageJ.

2.11 In vitro HUVECs migration experiment

Scratch test to assess the migration ability of HUVECs, which measures the expansion of HUVECs on margin. HUVECs were seeded at a density of 8×10^4 /well in a 12-well plate with FBS-free medium to form a confluent monolayer. After incubation for 1 d, a straight scratch was created by pipette tip, and the debris was gently washed twice with PBS. Then, each group treated with their corresponding nanomaterials at 37°C in the incubator. To quantify the closure of the scratch clearly, the cells were treated with 4% paraformaldehyde, incubated with 0.1% Triton X-100 (Sigma, USA), and then stained with 4',6-diamidino-2-phenylindole solution (DAPI, Invitrogen, USA). The difference between scratch wound at 0 h and 24 h was captured with an inverted microscope and the rate of cell migration was calculated as follows:

$$\text{HUVECs migration (\%)} = (W_{0h} - W_{12h}) / W_{0h},$$

where W_{0h} was the initial wound area and W_{12h} was the wound area after 12 h of incubation.

2.12 Cell viability assay

The MTT assay was used to determine the proliferation of HUVECs in leach liquor of each group materials and normal medium at different time. Firstly, HUVECs (5000 cells/well) were incubated in 96-well plates for 24 h. After starvation with fetal bovine serum (FBS)-free medium overnight, the culture medium was removed and replaced by the different groups' leach liquor respectively. They were incubated and the solution in each well was pipetted out at 6, 12 and 24 h. Subsequently, 20 μ L of MTT solution (5 mg/mL in FBS) was added into each well for 4 h at each time. Then, the supernatant was removed, and 150 μ L dimethyl sulfoxide (DMSO) was added into each well and incubated for 15 min in dark place. Finally, quantitative detection was performed on a microplate reader at 490 nm. In order to better mimic the microenvironment of bacterial infections in vivo, the cells were pretreated with 1 μ g/mL lipopolysaccharide (LPS) followed by different nanomaterials treatments for 24 hours, and cells treated with LPS alone were used as a positive control.

2.13 Western blot analysis

Cells or tissues around the wound were collected and homogenized with RIPA (EnoGene, China) buffer to collect supernatants. Equal amounts of proteins (15 μ g) separated on 10% polyacrylamide gels and transferred on PVDF membrane, which were blocked with 5% skim milk for 2 h. Then, the membranes were incubated with CD31, VEGF, bFGF, Tubulin antibodies followed by corresponding second antibodies for 2 h at indoor temperature. Immune reactivity was detected with super signal ultra-chemiluminescent reagent (Pierce Chemical, Rockford, IL, USA). Images were captured by Alpha Innotech Photodocumentation System (Alpha Innotech, Hayward, CA, USA). Quantification of the protein expression was performed by ImageJ software.

2.14 Immunofluorescence double labeling method

The leach liquor of each group was added into well plate. In each group, HUVECs and HaCaTs were washed 3 times with PBS and then were treated with 4% PFA for 40 min. After incubated with 0.1% Triton

X-100, cells were washed 3 times and blocked with 5% goat serum for 2 hours. Cells were also incubated with primary anti-bFGF (1:1000, CST, USA); anti-Tubulin (1:1000, CST, USA); anti-CD31 (1:500, abcam, UK); anti-VEGF (1:500, abcam, UK) overnight at 4°C. Subsequently, they were washed 3 times and incubated with Alexa Fluor 488 goat anti-rabbit IgG or Alexa Fluor 594 goat anti-mouse IgG (1:500, Thermo, USA) for 2 hours. Nuclei were stained with DAPI for 15 minutes. After washing, confocal laser scanning microscopy was used for further cells characterization.

2.15 Statistical analysis

All independent experiments were performed in triplicate in corresponding condition. All Graphs were rendered using GraphPad Prism software, version 6. One-way analysis of variance (ANOVA) with post hoc Tukey multiple comparison tests was used to analyze statistical significance. Differences between different groups at *P < 0.05, **P < 0.01, ***P < 0.001 were considered as statistically significant.

3. Results And Discussion

3.1 Preparation and characterization of EGCG-BPQDs@H

The black phosphorus quantum dots were obtained by the liquid-phase ultrasonic stripping method, and 500 mg of black phosphorus powder was put into 50 mL of N-methyl pyrrolidone (NMP), mixed and ground in a mortar. The mixture was sonicated in an ice bath for 4h, and then centrifuged at a speed of 12000 r/min for 20 min. The supernatant containing BPQDs was decanted. To verify the success of the composite preparation, a series of related experiments were carried out. Firstly, we used HRTEM to observe the morphological characteristics of EGCG-BPQDs. As shown in Fig. 1A, we can see homogeneous EGCG-BPQD nanoparticles. The insert in Fig. A is the image of one single magnified BPQD, the lattice fringes of the BPQD could be discriminated. The DLS indicated that the size of BPQDs is about 3 nm (Fig. 1B).

The results of FTIR spectra showed that the absorption peak at 1718 cm^{-1} and the broad absorption peak at $1400\text{--}1600\text{ cm}^{-1}$ were characteristic absorption peaks of -C=O and benzene of EGCG, 1100 cm^{-1} and 1250 cm^{-1} were P=O stretching vibration peak. It is proved that the prepared EGCG-BPQD@H already contains EGCG and BPQD (Fig. 1C). In addition, the synthetic hydrogels were tested by FTIR (Fig. S1). We tested the crystal form of the synthesized product by XRD. In Fig. 1D, the diffraction peaks at $\sim 16^\circ$, 34° and 52° corresponded well to the diffraction peaks of the (020), (040) and (060) crystal planes of BPQD, showing that BPQD still maintains a complete structure when it was fused to the hydrogel or bonded to EGCG (Fig. 1D). We demonstrated the successful preparation of EGCG-BPQDs by UV-vis spectroscopy. As shown in Fig. 1E. BPQDs exhibited a strong and sharp absorption peak at approximately 420 nm, which indicated the successful synthesis of high quality BPQDs [26]. Moreover, the characteristic absorption peaks of EGCG and BPQDs can be observed in EGCG-BPQDs, which again demonstrated that we have successfully synthesized EGCG-BPQDs. The fluorescence spectra demonstrated that the emission peaks of BPQDs and EGCG appear at 460 nm and 481 nm respectively,

and the peak of EGCG-BPQDs@H appears at 467 nm (Fig. 1F). These results indicated that we have successfully prepared EGCG-BPQDs and fused into hydrogels.

To verify the photothermal capability of EGCG-BPQDs@H in photothermal therapy, we irradiated EGCG-BPQDs@H with a NIR laser (2.5 W/cm², 808 nm) for 5 min and recorded the temperature change with a thermal imager (Fig. 1G and 1I). As shown in Fig. 1H, the temperature of EGCG-BPQDs@H and BPQDs@H increased to 53.5°C and 50.2°C, while the temperature of EGCG@H only changed 1.7°C, indicating that EGCG-BPQDs@H have excellent photothermal performance while its maximum photothermal conversion efficiency reaching 46.7% (Fig, S2). Finally, the stability of EGCG-BPQDs@H under cyclic light was also further explored. The samples were irradiated for the same duration and cycle (4 cycles, 5 minutes each cycle) and the highest temperature that the samples could reach after each cycle was recorded using a thermal imager (Fig. 1H). At the second cycle, the maximum temperature of the BPQDs began to decrease rapidly, reaching a maximum temperature of just 15.5°C by the fourth cycle, while the maximum temperature of the EGCG-BPQDs@H remained near 52°C and still maintained good photothermal properties. These results indicate that the hydrogels provided some protection to the BPQDs and reduced the degradation of the BPQDs.

The production of singlet oxygen is an important basis for assessing the effectiveness of photocatalytic effect with photosensitizers. We evaluated the ability of EGCG-BPQDs@H to produce singlet oxygen under NIR irradiation using ABDA solution. Under NIR conditions, the intensity of the absorption peak of the ABDA solution at 380 nm decreased sharply, indicating that the material produces a large amount of singlet oxygen (Fig. 1J). In contrast, the absorption spectra of the ABDA solution alone or the EGCG@H group did not change significantly under NIR irradiation (Fig. S3A-B). To further validate the conclusions, electron spin resonance measurements were performed to verify the ability of the material to produce singly linear oxygen. After 5 minutes of irradiation, typical electron spin resonance spectra were observed (Fig. 1K). The relative intensity of the electron spin resonance produced by EGCG-BPQDs@H was significantly higher than that of BPQDs@H for the same recording time, indicating that EGCG-BPQDs@H had a stronger ability to produce singlet oxygen. In vitro release experiments with EGCG@H were performed using dialysis bags and demonstrated that free EGCG showed a faster release rate. In contrast EGCG@H as well as EGCG-BPQDs@H could control the slow and smooth release of EGCG (Fig. S3C). UV-vis indicated that more EGCG was released from EGCG-BPQDs@H under NIR irradiation, which contributed to our further modulation of drug release (Fig. S3D).

3.2 In vitro antibacterial properties of EGCG-BPQDs@H

The agar spread assay was performed to evaluate antimicrobial capacity of different nanomaterials. After 37°C constant temperature cultivation, treatment with hydrogel did not show antibacterial effect for the tested bacterial. On the contrary, antibacterial rings of tested bacteria were clearly observed after treatment with BPQDs@H, EGCG@H or EGCG-BPQDs@H (Fig.2A). The diameters of EGCG-BPQDs@H group antibacterial zone towards *E. coli* and MRSA were ~23 mm, ~21 mm, respectively (Fig.2B and 2C), demonstrating its obvious antibacterial activity. These results presented the stronger antibacterial effect after treatment with EGCG-BPQDs@H, which was attributed to the synergistic relationship between EGCG

and BPQDs. In addition, experiments demonstrated that BPQDs can cause bacterial toxicity in the absence of NIR. MRSA and *E. coli* cells from different treatments were diluted and spread on the agar plates respectively. Next, the antibacterial effect of black phosphorous quantum dots was further investigated by the colony counts assay (Fig.2D and 2F). The results of colony count assay without NIR were in harmony with the antibacterial ring. Nevertheless, the bacteria viability in BPQDs@H+NIR treated

Figure 2. Antimicrobial efficacy of various methods on MRSA and *E. coli*. (A) Inhibition zones and (B, C) the corresponding statistical graphs of MRSA and *E. coli* with different treatments (1: hydrogel, 2: BPQDs@H, 3: EGCG@H, 4: EGCG-BPQDs@H). (D, F) Digital photos of bacterial colonies on agar plates with different treatments. (E, G) The corresponding bacterial colonies on agar plates were calculated.

groups were only 3.2% for *E. coli* and 11.3% for MRSA respectively (Fig. 2E and 2G).

These data also suggested the stronger antibacterial effect empowered by the phototherapy. Anyhow, these results indicated that neither EGCG-BPQDs@H nor photothermal treatment can completely eliminate the selected bacteria. On the contrary, especially in *E. coli*, almost no bacterial colonies were detected after combinational treatment EGCG-BPQDs@H under NIR irradiation. That is to say, the EGCG-BPQDs@H + NIR could more efficiently suppress bacterial viability and inhibit the growth of *E. coli* and MRSA. Briefly, the local thermal heat produced by nanomaterials under NIR irradiation was able to destroy bacteria by deactivating enzymes and disrupting metabolism in bacteria. Moreover, the NIR radiation provoked the release of EGCG from EGCG-BPQDs@H, which increased the local EGCG concentration. The high EGCG content affected the bacterial activity and led to bacterial death [27]. Therefore, cooperative treatment was a prominent strategy to eliminate bacteria.

3.3 evaluation of the integrity of bacteria

The bacterial survival rate was further identified through fluorescence staining assays to evaluate the antibacterial effect of the cooperative treatment. Fluorescence pictures of live/dead staining showed that only intense green fluorescence and no visible red fluorescence was observed in bacteria after treatment with normal hydrogels or with NIR only. By contrast, the BPQDs@H, EGCG@H, EGCG-BPQDs@H, BPQD@H+NIR, and EGCG@H+NIR treated bacterial emitted red fluorescence as well as green fluorescence, suggesting regional antibacterial efficacy was achieved (Fig.3A). Strongest red fluorescence could be detected in the group which the bacterial were treated with EGCG-BPQDs@H with NIR, indicating the potent antibacterial activity of the cooperative treatment (Fig.3B). SEM was used to observe the cellular morphological changes of MRSA following the different treatment (Fig.3C). As

Figure 3. Deformation of external structure of bacteria disposed of by EGCG-BPQDs@H. (A) Calcein-AM/PI staining images of MRSA in different treatment groups. Red spots signify dead bacteria, bar = 50µm. (B) The corresponding quantitative assay of live and dead bacteria. (C) The SEM images, bar = 500µm.

demonstrated in SEM pictures, it was found that bacterial remained typical spherical shape and intact smooth surface after treatment with normal hydrogel, NIR. In the case of the MRSA treated with

BPQDs@H, EGCG@H, EGCG-BPQDs@H, BPQD@H + NIR, or EGCG@H + NIR, obvious disruption appeared on their original morphology, indicating their surface became slightly rough and fragmentary. Whereas the structure of bacteria was distorted and displayed more serious damage after combining with EGCG-BPQDs@H under NIR irradiation, implying the strongest antibacterial effect of the cooperative treatment. Besides the special photothermal property of BPQDs can convert near-infrared light into local high temperature to denature the enzymes in the bacteria, the phenolic hydroxyl of EGCG could bind to the phospholipid bilayer of bacteria and the amino and carboxyl groups in bacterial membrane proteins, which was reported to disrupt the integrity of the bacterial membrane [28].

3.4 Antibacterial mechanism exploration in vitro

In addition to the above results, in order to explore the antibacterial mechanism and antibacterial effect, the active oxygen generated under radiation was further examined. DCFH-DA was used to monitor the generation of ROS after different treatments on MRSA. As a potential photocatalyst, black phosphorous nanomaterials could generate numerous singlet oxygen (1O_2), which can introduce reactive oxygen-dependent oxidative stress and membrane damage [29–32]. It was observed that little green fluorescence of the bacteria was detected after treatment with normal saline or NIR. Whereas the laser irradiation significantly enhanced ROS production in BPQDs@H and EGCG-BPQDs@H treated group. More importantly, much higher level of ROS was generated in EGCG-BPQDs@H treated group partly attributed to the spontaneous slow release of EGCG. Meanwhile, comparing with EGCG-BPQDs@H group, ROS production was obviously upregulated in EGCG-BPQDs@H + NIR group due to the EGCG release and high temperature (Fig. 4A and 4C). Since the rupture of the membrane causes cytoplasm to leak, the degree of protein leakage can be used as a response to the antibacterial effect [33]. We further evaluated the leakage of intracellular protein after exposure of different groups. As shown in Fig. S4, the leakage of proteins from the bacteria treated with the combination was significantly reduced. Nevertheless, in the other groups only relatively weak changes were observed, indicating that EGCG-BPQDs@H caused severe disruption of the bacterial cell membrane under NIR irradiation.

Biofilms have further weakened the therapeutic effect due to their resistance to antibiotic therapy [34]. Therefore, the antibacterial activity of EGCG-BPQDs@H against the MRSA biofilm was further test. The darker the blue, the more biofilm stained by crystal violet. Limited radicalization was observable following normal saline or BPQDs@H treatment alone, and the radicalization activity was not related to NIR light (Fig.4B). As shown in Fig.4D, the corresponding absorbance and solution color of group treated with EGCG-BPQDs@H+NIR were the least of all the treating sets, suggesting that the synergistic system of EGCG-BPQDs@H+NIR has an efficiency against biofilm. In brief, simply NIR radiation, EGCG@H or the BPQDs@H cannot kill bacteria effectively. Under the NIR irradiation, the photothermal and photocatalytic properties of EGCG-BPQDs@H could be activated, and together with increased release of EGCG, which exerted additional antibacterial effect to bacteria system. EGCG-BPQDs@H excited by NIR laser present a higher bactericidal efficiency than EGCG-BPQDs@H. This enhancement might due to the synergistic effect of photothermal and active oxygen sterilization. Comparison between EGCG-BPQDs@H and

BPQDs@H also affirmed the positive efficacy of EGCG, and there was no significant change before and after NIR illumination. Accordingly, the NIR

Figure 4. The investigation of antibacterial mechanisms. (A) Fluorescent photographs of ROS level in MRSA with various treatments in vitro, stained by DCFH-DA, bar = 100 μ m. (B) Crystalline violet-stained biofilm. (E) Images of MRSA biofilms stained with crystal violet, bar = 200 μ m. (C) Consequential statistics of histograms indicating religious ROS activity levels. (D) Absorbance of biofilm in different groups.

regulated photothermal, ROS and release promoting synergetic therapy could be used to completely combat multidrug-resistant bacterial infections.

3.5 Promoting migration and proliferation effects of EGCG-BPQDs@H in vitro

It is commonly accepted that endothelial cell migration is one of the critical steps in angiogenesis [35]. EGCG is considered to have a superior impact in accelerating wound healing by the virtue of antibacterial, anti-inflammatory and facilitating angiogenesis [36–38]. Therefore, the regenerative ability of EGCG-BPQDs@H was further investigated through HUVECs. Following the different treatments of cells scratch, the migration extent revealed difference (Fig. 5A). Compared with other groups, significant cell migration was detected in EGCG-BPQDs@H group after 24 hours incubation (Fig. 5B). The wound area in EGCG-BPQDs@H group decreased dramatically by 52.8%, while only 43.1%, 38.3% and 17.6% of the wound decreased in the EGCG@H, BPQDs@H and control group. Since the cytocompatibility is critical for serving as wound healing, as it directly contacts with wound tissue. Cell proliferation was also determined by MTT assay. The cell proliferation was sustainedly increased optical density (Fig. 5C). The proliferation of HUVECs after treatment of EGCG-BPQDs@H were significantly faster than other groups after 12- and 24-hours incubation. The migration and proliferation among HUVECs indicated nanomaterials have good biocompatibility and the ability to improve wound healing, which could be attributed to the sustained release of EGCG offering an appropriate microenvironment for distribution. Meanwhile, we evaluate the capacity of nanomaterials to promote epithelial by detecting the expression of basic fibroblast growth factor (bFGF) in HaCaT cells. It is widely accepted that bFGF is a kind of growth factor that takes a significant role in therapy of skin trauma, neovascularization and tissue regeneration [39]. Immunofluorescence observed on CLSM revealing expression of bFGF protein in HaCaTs was much higher in EGCG-BPQDs@H treatment (Fig. 5D).

Through western blot (Fig. 5E) and relative western blot quantitative analysis (Fig. 5F), enhanced expression of bFGF was discovered in EGCG-BPQDs@H group. Although the bFGF protein levels of other signal groups were higher than the control group, but both were lower than EGCG@BOQDs@H group, indicating the synergistic properties of black phosphorus quantum dots and EGCG. Therefore, the experimental results confirmed that the nanomaterials had the potential to accelerate epithelial healing by promoting the expression of bFGF in epithelial cells.

3.6 EGCG-BPQDs@H facilitated vascularization

Angiogenesis is the process of developing new capillaries to form the original microvasculature, which is an indispensable stage in wound healing [40]. Total processes involved the proliferation, migration, alignment, and the germination of endothelial cells, as well as the formation of connections between cells, tubular structures, and lumina [41]. We conducted the Matrigel experiment to simulate the angiogenesis of endothelial cells on connective tissue membrane. As shown in Fig. 6A, HUVECs incubated on the Matrigel after different materials treatments formed tube networks and mesh-like circles to a different degree. The HUVECs treated with EGCG@H and EGCG-BPQDs@H exhibited more notable angiogenesis indexes. Furthermore, longer total lengths, enhanced number of nodes were observed in EGCG-BPQDs@H treatment (Fig. 6B and C). These results identified that EGCG-BPQDs@H served as an ideal extracellular matrix to facilitated the tubule formation of endothelial cells in vitro, which may accelerate endothelization and angiogenesis in impaired tissues.

To further identify our inference, we performed CLSM and western blot to examine the expression of the angiogenesis-associated proteins. It has been widely demonstrated that CD31 and VEGF can assess the level of angiogenesis. The highly expressed CD31 indicate the tight junctions between endothelial cells and involved in the formation of blood vessels [42]. EGCG@H exhibited a modicum improvement in expression of CD31. By contrast, EGCG-BPQDs@H further enhanced the expression level of CD31 (Fig.6D). Moreover, the result of western blot acted in accordance with immunofluorescence staining (Fig.6E). The expression of CD31 in the group with

Figure 6. Angiogenic tubular formation and relative protein expression of endothelial cells in vitro. (A) Tubular formation on Matrigel and digital analysis conversion of HUVECs in different treatments, bar = 100 μ m. (B, C) Total of length and the number of nodes were quantified. (D) CLSM images of the expression analysis of CD31, bar = 25 μ m. (E) The expression level of CD31 and VEGF protein. (F) Quantification analysis of the CD31 and VEGF protein. *P < 0.05, **P < 0.01, ***P < 0.001.

treatment of EGCG@BOQDs@H was remarkably improved compared to other groups (Fig. 6F). Undoubtedly, expression of VEGF in EGCG-BPQDs@H treatment was higher than other groups. All these results suggested that we had proved once again that EGCG-BPQDs@H could ameliorate wound healing through promoting angiogenesis according to the relative protein expression. In combination with these findings, our study provides supporting evidence for the use of NIR-responsive, synergistic antimicrobial, sustained-release hydrogels of EGCG-modified BPQDs to promote MIDBW healing. To further investigate the healing effect in more detail, we carried out experiments in vivo.

3.7 In vivo assessment of burn-wound healing

To further explore the therapeutic benefits of EGCG-BPQDs@H in burn-wound healing in vivo, the digital photographs of burn-wound showed male Sprague-Dawley diabetic rats infected burning wounds (Fig. 7A). The burn-wounds of diabetic rats treated with EGCG-BPQDs@H with or without NIR revealed accelerated wound closure in the continued bacterial infected burn-wound healing experiment (Fig. 7B). More specifically, relative wound area on day 21 exhibited that local EGCG-BPQDs@H with NIR irradiation application leading to 92.4% wound closure, which were conspicuously higher than the control group

(61.1%) (Fig. 7C). Remarkably, the elevated temperature induced by photothermal effect was detected upon NIR irradiation. The highest temperature of wound region treated with BPQDs@H or EGCG-BPQDs@H was $\sim 55^{\circ}\text{C}$ after 5 minutes' irradiation, revealing prominent photothermal performance of black phosphorus quantum dots (Fig. 7D).

Despite one major concern about photothermal therapy (PTT) is that local hyperpyrexia may cause secondary injury to burn-wound, the impairment to cells around the wound caused PTT is far less serious than that caused by bacterial infection. This is acceptable for PTT-mediated improvement of blood flow and increase oxygen supply to promote burn-wound healing. In contrast, the trauma area in control or EGCG@H groups showed temperature increase of only 1.7°C and 2.0°C . Moreover, no significant body weight fluctuations were observed in all groups during the treatment period (Fig. 7E), indicating the satisfactory bio-safety to these tested nanomaterials. In the meantime, obvious healing effect can also be observed in the treatment of EGCG-BPQDs@H compared with other single treatment groups. While EGCG@BPQDs@H + NIR group indicating the minimum wound area and fastest healing rate, which revealed the EGCG-BPQDs@H could be used for applying the drug-resistant bacterial infected diabetic wound in vivo with assistance of the photothermal and photocatalytic effects. Next, to verify the in vivo antimicrobial activity, we collected MRSA from the wound skin and performed a bacterial colony count test using the LB agar plate smear method. As shown in Fig. S5A, few colonies were seen in the EGCG-BPQDs@H + NIR group, and the results were consistent with in vitro experiments. And by H&E staining (Fig. S5B), a large number of inflammatory cells were found in the wounds treated with the control group. After treatment with EGCG-BPQDs@H with NIR, there was a significant reduction in the number of inflammatory cells in the wounds relative to the other groups.

To observe the histological changes in wound healing, H&E and Masson staining were performed to study the mechanism behind this process. Compared with other groups, control and BPQDs@H groups could not develop intact epidermal tissue. EGCG@H and EGCG-BPQDs@H groups had basically completed the procedure of

Figure 7. Evaluation effects of accelerating diabetic infected burn-wound in vivo. (A) Images of infected burn-wound healing at different times, bar = 5mm. (B) Traces of wound-bed closure during 21 days for each treatment. (C) Corresponding statistical graph of relative wound area from each group with different treatments. (D) Photothermal images of rats treated with hydrogel, BPQDs@H, EGCG@H and EGCG-BPQDs@H with NIR irradiation at different times. (E) Changes of body weight of the rats.

re-epithelialization. The epithelium of the EGCG-BPQDs@H with NIR group was smoother and more regulated than of the EGCG-BPQDs@H group, and follicles began to develop around the wound (Fig. 8A). Matson staining was then applied to samples from different groupings to reflect the deposition of collagen in the sarcomeres. As a result, only a few of collagen fiber bundles were formed in the control and BPQDs@H groups, and there was still large spaced and a loose reticular arrangement between the collagen fibers and skin tissue remaining. In contrast, EGCG-BPQDs@H group had an intact epidermal structure and dense, regular collagen fibers with a larger area of collagen deposition at the wound

(Fig. 8B). Subsequently, western blot analysis revealed that EGCG-modified BPQDs had increased the expression of key signaling molecules in the PI3K/AKT and ERK1/2 pathways (Fig. 8C). Quantitative analysis revealed the phosphoinositide 3-kinase (PI3K), protein kinase B (AKT) and extracellular signal-regulated kinase (ERK1/2) were significantly increased in the EGCG-BPQDs@H group compared to the control group (Fig. 8D). These signaling pathways direct cells proliferation and differentiation, which was attributed to the stimulative effect of the phosphate/phosphonate ions following the degradation of BPQDs. Figure 8E summarizes the previous findings on how nanomaterials induce signaling pathways to direct cell proliferation and differentiation.

3.8 Biological safety in vivo

The results presented above fully attested the prominent properties and potential of EGCG-BPQDs@H with NIR irradiation treatment in antibacterial activity and wound healing. Meanwhile, it is quite crucial to assess the biocompatibility of combined photothermal therapy in vivo for its practical application. Due to the characteristics of nanomaterials in direct contact with the burn-wound, blood biochemical analysis and histological examination were applied to evaluate the biocompatibility of the cooperative treatment *in vivo*. BP has been widely used in drug delivery with high biocompatibility [43]. Additionally, biodegradation products of BP are phosphate ions and phosphonates, which are normally present in the blood [44]. Biochemistry analyses carried out for blood at the twenty-first day. The liver function indexes (such as ALT and AST) and kidney function indexes (such as BUN and CREA) in the EGCG-BPQDs@H + NIR system were in the normal range (Fig. 9A). Subsequently, for EGCG-BPQDs@H + NIR system, H&E staining did not detect apparent inflammation and necrosis in normal anatomical structure of various organs after treatment (Fig. 9B). All these results strongly demonstrated the EGCG-BPQDs@H with NIR irradiation system could be competent for a safe and effective therapeutic strategy to accelerate infected burn-wound healing.

4. Conclusion

In summary, the present work successfully constructed photocatalytic, photothermal effects of EGCG modified black phosphorus quantum dots as multifunctional nanoplateforms and evaluated their antibacterial ability and wound healing activity in MRSA-infected wounds under diabetic conditions. The resulted EGCG-BPQDs present an effective sterilization rate of 88.6% for MRSA. Combining the photothermal effect of our sterilization depot, it promotes the release of EGCG and EGCG-BPQDs@H could produce $^1\text{O}_2$ in the case of NIR light. Molecular biology analysis demonstrated that EGCG-BPQDs significantly upregulated CD31 nearly 4-fold and basic fibroblast growth factor (bFGF) nearly 2-fold, which were beneficial for promoting proliferation of vascular endothelial cells and skin epidermal cells. Under NIR irradiation, EGCG-BPQDs hydrogel (EGCG-BPQDs@H) treated MIDBW area could rapidly raise temperature up to 55°C for sterilization. The MIDBW closure rate of rat after 21 days of treatment was 92.4%, much better than that of 61.1% of the control group. The engineered EGCG-BPQDs were found to promote MIDBW healing by triggering the PI3K/AKT and ERK1/2 signaling pathways, which could

enhance cell proliferation and differentiation. In addition, intravenous circulation experiment showed good biocompatibility of EGCG-BPQDs, no obvious damage to rat major organs were observed. The obtained results demonstrate that EGCG-BPQDs are promising multifunctional nanoplateforms for MIDBW healing. Thus, the results of this study provide strong evidence for the clinical applicability of EGCG-BPQDs@H for the successful treatment of wounds in complex disease conditions such as diabetes with infected burn wounds.

Abbreviations

MRSA: Methicillin-resistant *Staphylococcus aureus*; EGCG: Epigallocatechin gallate; BPQDs: Black phosphorus quantum dots; NIR: Near infrared; bFGF: basic fibroblast growth factor; BP: Black phosphorus; $^1\text{O}_2$: Singlet oxygen; *E. coli*: Gram-negative bacteria *Escherichia coli*; DMEM: Dulbecco's modified Eagle's medium; MTT: 3-(4,5-Dimethylthiazol-2-yl)-2,5-diphenyl tetrazolium bromide; FBS: Fetal bovine serum; HaCat: Human skin keratinocytes cells; HUVEC: human umbilical vein endothelial cells; ABDA: The 2,2'-bis(anthracene-9,10-diylbis(methylene))-dimalonic acid; NMP: 1-methyl-2-pyrrolidone; DLS: dynamic laser scattering; TEM: Transmission electron microscope; CLSM: Confocal laser scanning microscopy; STZ: Streptozotocin; SEM: Scanning electron microscope; DCFH-DA: 2',7'-dichlorodihydrofluorescein diacetate; DAPI: 4',6-diamidino-2-phenylindole solution; DMSO: Dimethyl sulfoxide; ALT: Alanine aminotransferase; AST: Aspartate aminotransferase; CREA: Creatinine.

Declarations

Acknowledgements

Not applicable.

Author's contributions

SBX, LNC, SCH: conception and design of the experiment, as well as manuscript writing; YNH, XJZ, SBX: collection an assembly of data and data interpretation; SBX, SCH: perform the experiment and edit manuscript. ZHC, XLR, XFM: conception and design, financial support and the preparation. All authors read and approved the final manuscript.

Funding

This work was supported by National Natural Science Foundation of China (No. 82072076, 82072165 and 81871556), and Young Top Talents in Xing Liao Talents Program of Liaoning Province (XL YC1807183).

Availability of data and materials

The datasets used and/or analyzed during the current study are available from the corresponding author on reasonable request.

Ethics approval and consent to participate

Animal care conformed to institutional guidelines. All animal studies were agreed by the Institutional Ethics Committee of Jinzhou Medical University.

Competing interests

No potential conflicts of interest were disclosed.

Consent for publication

All authors agree to be published.

Author details

Jinzhou Medical University, Jinzhou, 121001, Liaoning, China.

References

- [1] Cao B, Xiao F, Xing D, et al. Polyprodrug Antimicrobials: Remarkable Membrane Damage and Concurrent Drug Release to Combat Antibiotic Resistance of Methicillin-Resistant *Staphylococcus aureus*. *Small*, 2018, 14(41): 1802008.
- [2] Ito K, Saito A, Fujie T, et al. Sustainable antimicrobial effect of silver sulfadiazine-loaded nanosheets on infection in a mouse model of partial-thickness burn injury. *Acta biomaterialia*, 2015, 24: 87-95.
- [3] Gould K. Antibiotics: from prehistory to the present day. *Journal of Antimicrobial Chemotherapy*, 2016, 71(3): 572-575.
- [4] Hussain S, Joo J, Kang J, et al. Antibiotic-loaded nanoparticles targeted to the site of infection enhance antibacterial efficacy. *Nature biomedical engineering*, 2018, 2(2): 95-103.
- [5] Dang C N, Prasad Y D M, Boulton A J M, et al. Methicillin-resistant *Staphylococcus aureus* in the diabetic foot clinic: a worsening problem. *Diabetic Medicine*, 2003, 20(2): 159-161.
- [6] Katsoulis E, Bissell I, Hargreaves D G. MRSA pyogenic flexor tenosynovitis leading to digital ischaemic necrosis and amputation. *Journal of Hand Surgery*, 2006, 31(3): 350-352.
- [7] Farha M A, French S, Stokes J M, et al. Bicarbonate alters bacterial susceptibility to antibiotics by targeting the proton motive force. *ACS infectious diseases*, 2017, 4(3): 382-390.
- [8] Shakya S, He Y, Ren X, et al. Ultrafine silver nanoparticles embedded in cyclodextrin metal-organic frameworks with GRGDS functionalization to promote antibacterial and wound healing application. *Small*, 2019, 15(27): 1901065.

- [9] Yu P, Han Y, Han D, et al. In-situ sulfuration of Cu-based metal-organic framework for rapid near-infrared light sterilization. *Journal of hazardous materials*, 2020, 390: 122126.
- [10] Wang Y, Yu Y, Guo J, et al. Bio-Inspired Stretchable, Adhesive, and Conductive Structural Color Film for Visually Flexible Electronics. *Advanced Functional Materials*, 2020, 30(32): 2000151.
- [11] Xu Z, Qiu Z, Liu Q, et al. Converting organosulfur compounds to inorganic polysulfides against resistant bacterial infections. *Nature communications*, 2018, 9(1): 1-13.
- [12] Zhang X, Chen G, Yu Y, et al. Bioinspired Adhesive and Antibacterial Microneedles for Versatile Transdermal Drug Delivery. *Research*, 2020, 2020.
- [13] Xiang Y, Mao C, Liu X, et al. Rapid and superior bacteria killing of carbon quantum dots/ZnO decorated injectable folic acid-conjugated PDA hydrogel through dual-light triggered ROS and membrane permeability. *Small*, 2019, 15(22): 1900322.
- [14] Krizsan A, Volke D, Weinert S, et al. Insect-derived proline-rich antimicrobial peptides kill bacteria by inhibiting bacterial protein translation at the 70 S ribosome. *Angewandte Chemie International Edition*, 2014, 53(45): 12236-12239.
- [15] Xie K, Zhou Z, Guo Y, et al. Long-Term Prevention of Bacterial Infection and Enhanced Osteoinductivity of a Hybrid Coating with Selective Silver Toxicity. *Advanced healthcare materials*, 2019, 8(5): 1801465.
- [16] Li Z, Fu Q, Ye J, et al. Ag⁺-Coupled Black Phosphorus Vesicles with Emerging NIR-II Photoacoustic Imaging Performance for Cancer Immune-Dynamic Therapy and Fast Wound Healing. *Angewandte Chemie International Edition*, 2020, 59(49): 22202-22209.
- [17] Zhang X, Chen G, Liu Y, et al. Black phosphorus-loaded separable microneedles as responsive oxygen delivery carriers for wound healing. *ACS nano*, 2020, 14(5): 5901-5908.
- [18] Zhang H, Zhang Z, Zhang H, et al. Protein-Based Hybrid Responsive Microparticles for Wound Healing. *ACS Applied Materials & Interfaces*, 2021.
- [19] Han D, Han Y, Li J, et al. Enhanced photocatalytic activity and photothermal effects of Cu-doped metal-organic frameworks for rapid treatment of bacteria-infected wounds. *Applied Catalysis B: Environmental*, 2020, 261: 118248.
- [20] Huang B, Tan L, Liu X, et al. A facile fabrication of novel stuff with antibacterial property and osteogenic promotion utilizing red phosphorus and near-infrared light. *Bioactive materials*, 2019, 4: 17-21.
- [21] Li J, Liu X, Tan L, et al. Zinc-doped Prussian blue enhances photothermal clearance of *Staphylococcus aureus* and promotes tissue repair in infected wounds. *Nature communications*, 2019, 10(1): 1-15.

- [22] Mao C, Xiang Y, Liu X, et al. Repeatable photodynamic therapy with triggered signaling pathways of fibroblast cell proliferation and differentiation to promote bacteria-accompanied wound healing. *ACS nano*, 2018, 12(2): 1747-1759.
- [23] Chen Z, Wang C, Chen J, et al. Biocompatible, functional spheres based on oxidative coupling assembly of green tea polyphenols. *Journal of the American Chemical Society*, 2013, 135(11): 4179-4182.
- [24] Chen G, He L, Zhang P, et al. Encapsulation of green tea polyphenol nanospheres in PVA/alginate hydrogel for promoting wound healing of diabetic rats by regulating PI3K/AKT pathway. *Materials Science and Engineering: C*, 2020, 110: 110686.
- [25] Zhang P, He L, Zhang J, et al. Preparation of novel berberine nano-colloids for improving wound healing of diabetic rats by acting Sirt1/NF- κ B pathway. *Colloids and Surfaces B: Biointerfaces*, 2020, 187: 110647.
- [26] Batmunkh M, Myekhlai M, Bati A S R, et al. Microwave-assisted synthesis of black phosphorus quantum dots: efficient electrocatalyst for oxygen evolution reaction. *Journal of Materials Chemistry A*, 2019, 7(21): 12974-12978.
- [27] Gao Q, Zhang X, Yin W, et al. Functionalized MoS₂ nanovehicle with near-infrared laser-mediated nitric oxide release and photothermal activities for advanced bacteria-infected wound therapy. *Small*, 2018, 14(45): 1802290.
- [28] Akagawa M, Shigemitsu T, Suyama K. Production of hydrogen peroxide by polyphenols and polyphenol-rich beverages under quasi-physiological conditions. *Bioscience, biotechnology, and biochemistry*, 2003, 67(12): 2632-2640.
- [29] Lucky S S, Muhammad Idris N, Li Z, et al. Titania coated upconversion nanoparticles for near-infrared light triggered photodynamic therapy. *ACS nano*, 2015, 9(1): 191-205.
- [30] Hu Y, Huang S, Zhao X, et al. Preparation of Photothermal Responsive and ROS generative Gold Nanocages for Cancer Therapy. *Chemical Engineering Journal*, 2021: 129744.
- [31] Xiong Z, Zhang X, Zhang S, et al. Bacterial toxicity of exfoliated black phosphorus nanosheets. *Ecotoxicology and environmental safety*, 2018, 161: 507-514.
- [32] Chang L, Huang S, Zhao X, et al. Preparation of ROS active and photothermal responsive hydroxyapatite nanoplatforms for anticancer therapy. *Materials Science and Engineering: C*, 2021, 125: 112098.
- [33] Zhao R, Kong W, Sun M, et al. Highly stable graphene-based nanocomposite (GO-PEI-Ag) with broad-spectrum, long-term antimicrobial activity and antibiofilm effects. *ACS applied materials & interfaces*, 2018, 10(21): 17617-17629.

- [34] Zhao Y, Dai X, Wei X, et al. Near-infrared light-activated thermosensitive liposomes as efficient agents for photothermal and antibiotic synergistic therapy of bacterial biofilm. *ACS applied materials & interfaces*, 2018, 10(17): 14426-14437.
- [35] Yin K J, Olsen K, Hamblin M, et al. Vascular endothelial cell-specific microRNA-15a inhibits angiogenesis in hindlimb ischemia. *Journal of Biological Chemistry*, 2012, 287(32): 27055-27064.
- [36] Chen Z, Duan J, Diao Y, et al. ROS-responsive capsules engineered from EGCG-Zinc networks improve therapeutic angiogenesis in mouse limb ischemia. *Bioactive materials*, 2021, 6(1): 1-11.
- [37] Xu Z, Li J, Zhou X, et al. The combined use of tea polyphenols and lactobacillus plantarum ST8SH bacteriocin in a rabbit model of infection following femoral fracture with internal fixation. *Medical science monitor: international medical journal of experimental and clinical research*, 2019, 25: 312-317.
- [38] Gao X, Xu Z, Liu G, et al. Polyphenols as a versatile component in tissue engineering. *Acta Biomaterialia*, 2021, 119: 57-74.
- [39] Zhu J, Zhang M, Gao Y, et al. Tetrahedral framework nucleic acids promote scarless healing of cutaneous wounds via the AKT-signaling pathway. *Signal Transduction and Targeted Therapy*, 2020, 5(1): 1-11.
- [40] Tonnesen M G, Feng X, Clark R A F. Angiogenesis in wound healing. *Journal of Investigative Dermatology Symposium Proceedings*. Elsevier, 2000, 5(1): 40-46.
- [41] Nakatsu M N, Sainson R C A, Aoto J N, et al. Angiogenic sprouting and capillary lumen formation modeled by human umbilical vein endothelial cells (HUVEC) in fibrin gels: the role of fibroblasts and Angiopoietin-1. *Microvascular research*, 2003, 66(2): 102-112.
- [42] Wang C, Liang C, Wang R, et al. The fabrication of a highly efficient self-healing hydrogel from natural biopolymers loaded with exosomes for the synergistic promotion of severe wound healing. *Biomaterials science*, 2020, 8(1): 313-324.
- [43] Choi J R, Yong K W, Choi J Y, et al. Black phosphorus and its biomedical applications. *Theranostics*, 2018, 8(4): 1005-1026.
- [44] Shao J, Xie H, Huang H, et al. Biodegradable black phosphorus-based nanospheres for in vivo photothermal cancer therapy. *Nature communications*, 2016, 7(1): 1-13.

Figures

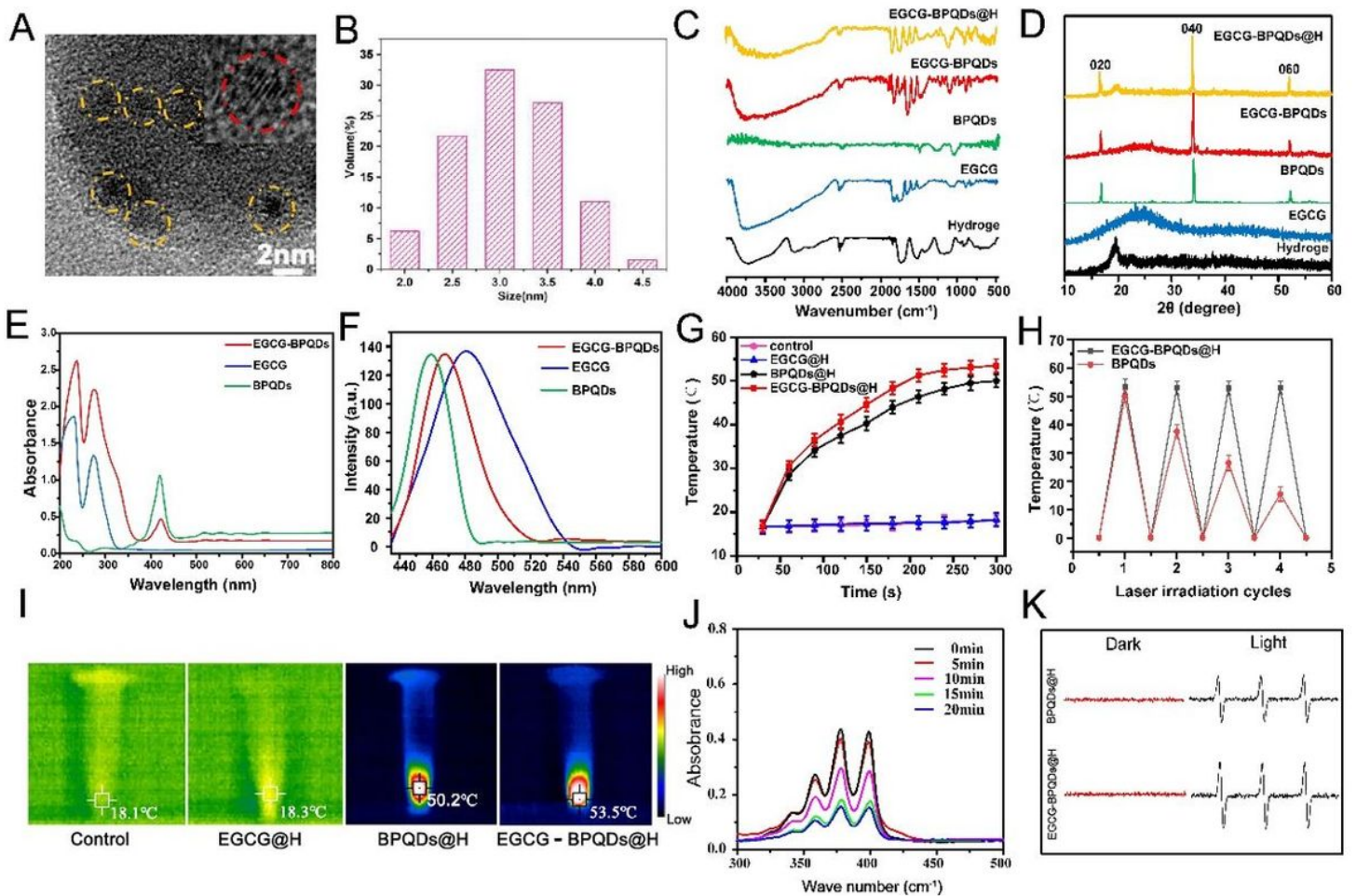


Figure 1

Characterization of BPQDs@H, EGCG@H, EGCG-BPQDs@H. (A) HRTEM images and (B) DLS size distribution of EGCG-BPQDs; the insert in A is the image of one single magnified BPQD. (C) FTIR spectra, (D) XRD, (E) UV-vis and (F) fluorescence emission ($\lambda_{\text{exc}} = 400\text{nm}$) of samples. (G) Temperature rise curves of four groups of samples within 5 minutes. (H) The thermal curves of BPQDs@H and EGCG-BPQDs@H after repeated laser irradiation ($n = 3$). (I) Infrared thermography images of samples under 808 nm laser irradiation for 5 minutes. (J) ABDA solution containing EGCG-BPQDs@H after irradiation for different times. (K) The ESR spectra of BPQDs@H and EGCG-BPQDs@H after being in the dark or irradiated with light for 10 min.

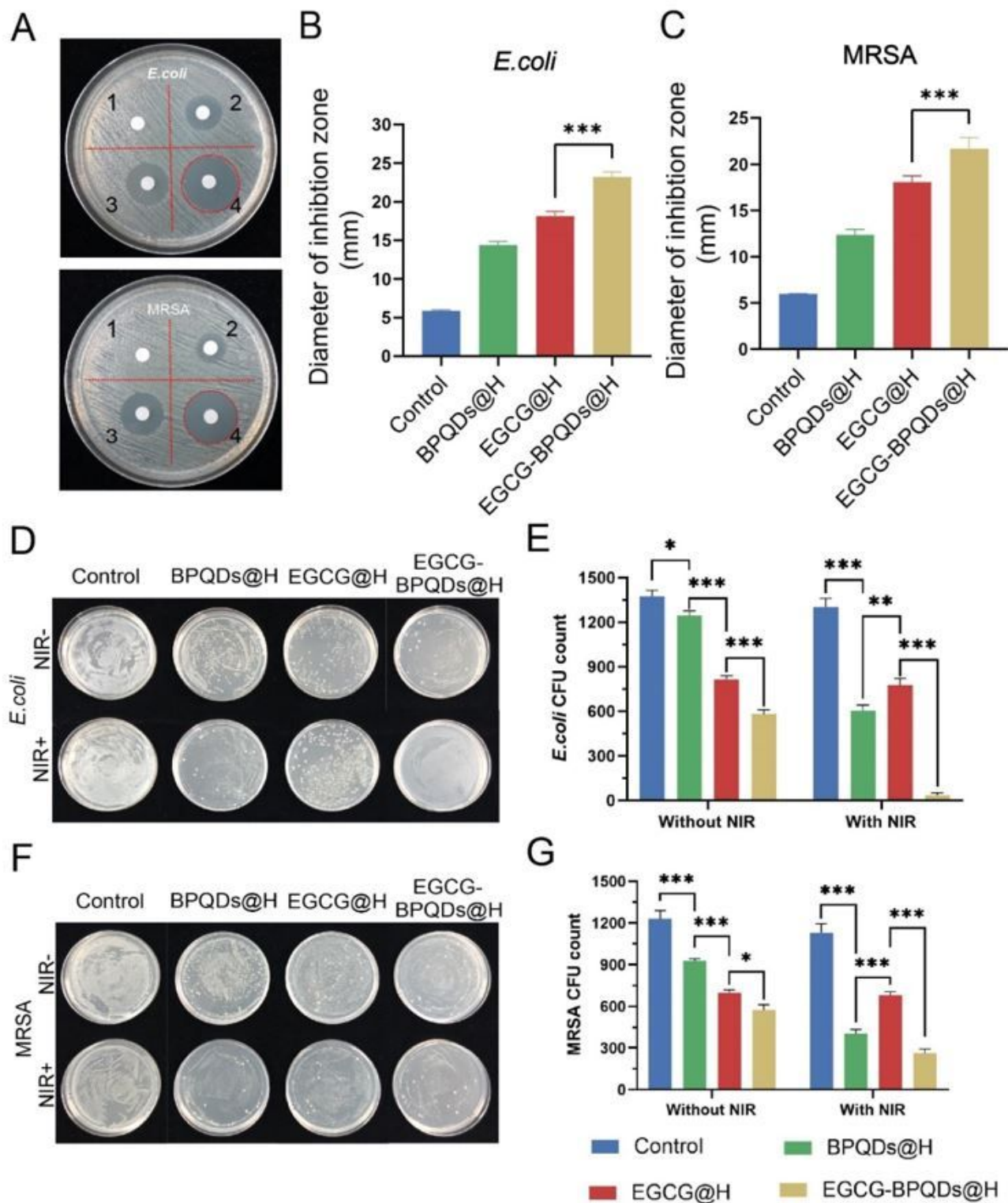


Figure 2

Antimicrobial efficacy of various methods on MRSA and *E. coli*. (A) Inhibition zones and (B, C) the corresponding statistical graphs of MRSA and *E. coli* with different treatments (1: hydrogel, 2: BPQDs@H, 3: EGCG@H, 4: EGCG-BPQDs@H). (D, F) Digital photos of bacterial colonies on agar plates with different treatments. (E, G) The corresponding bacterial colonies on agar plates were calculated.

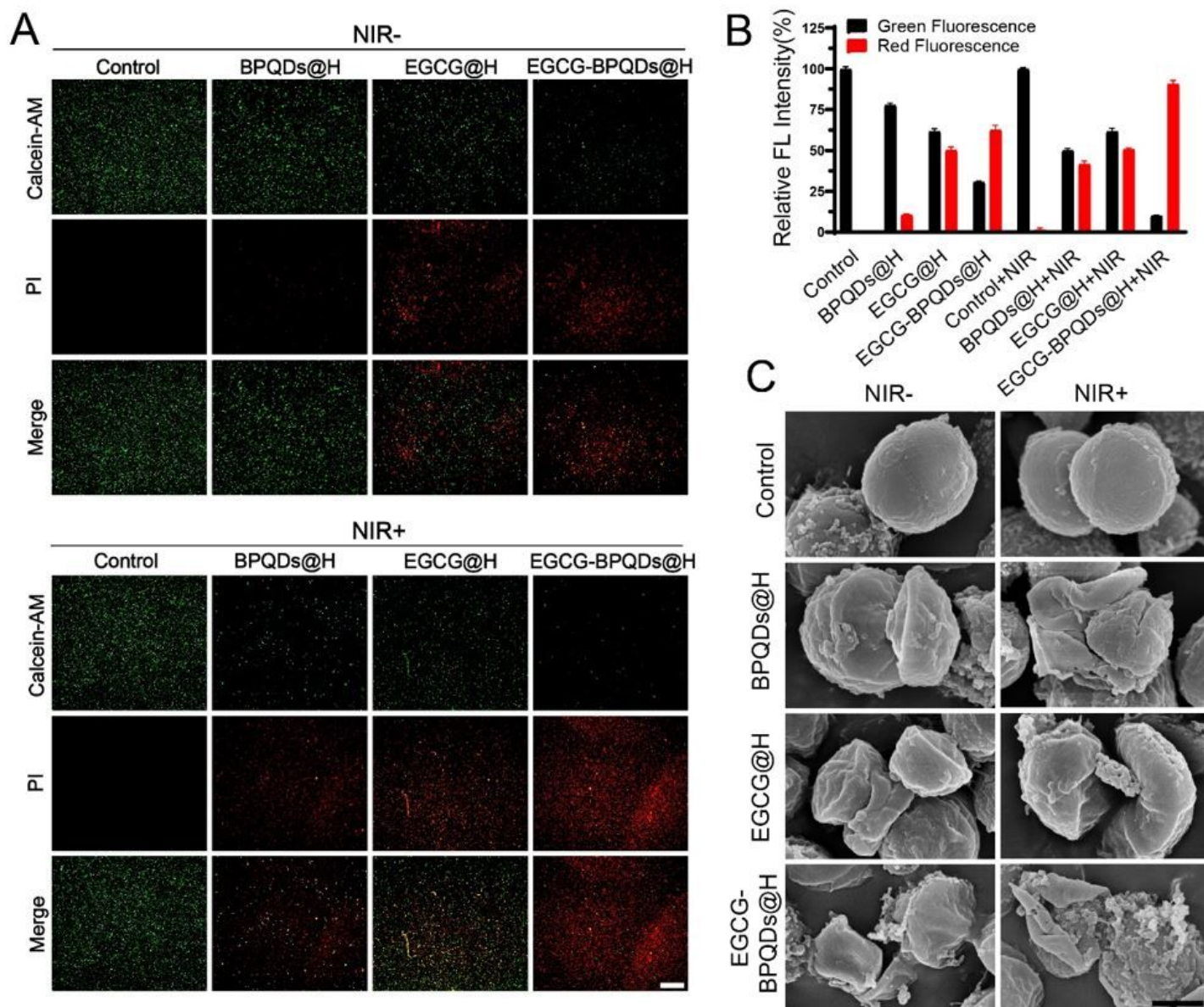


Figure 3

Deformation of external structure of bacteria disposed of by EGCG-BPQDs@H. (A) Calcein-AM/PI staining images of MRSA in different treatment groups. Red spots signify dead bacteria, bar=50 μ m. (B) The corresponding quantitative assay of live and dead bacteria. (C) The SEM images, bar=500 μ m.

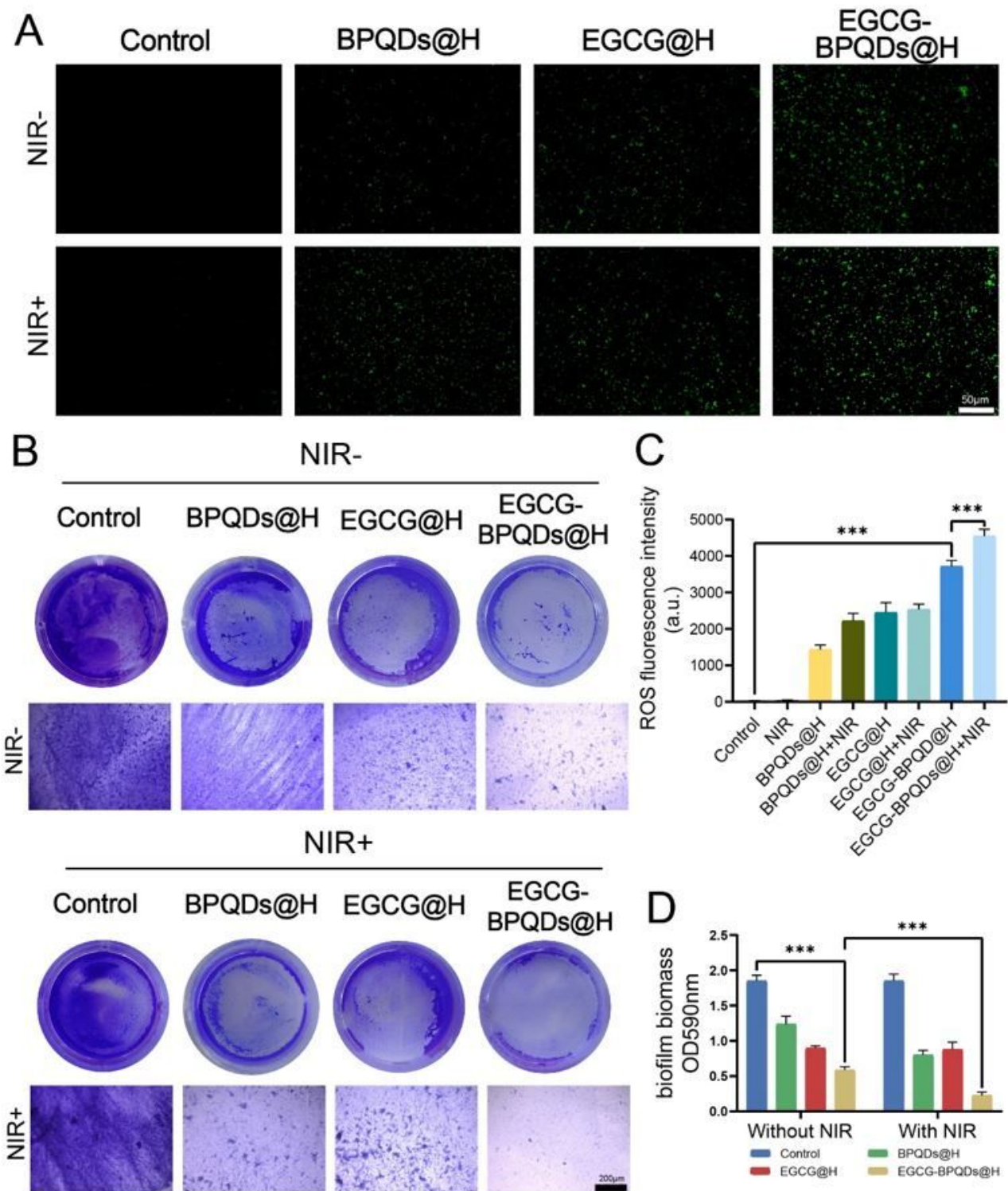


Figure 4

The investigation of antibacterial mechanisms. (A) Fluorescent photographs of ROS level in MRSA with various treatments in vitro, stained by DCFH-DA, bar=100µm. (B) Crystalline violet-stained biofilm. (E) Images of MRSA biofilms stained with crystal violet, bar=200µm. (C) Consequential statistics of histograms indicating religious ROS activity levels. (D) Absorbance of biofilm in different groups.

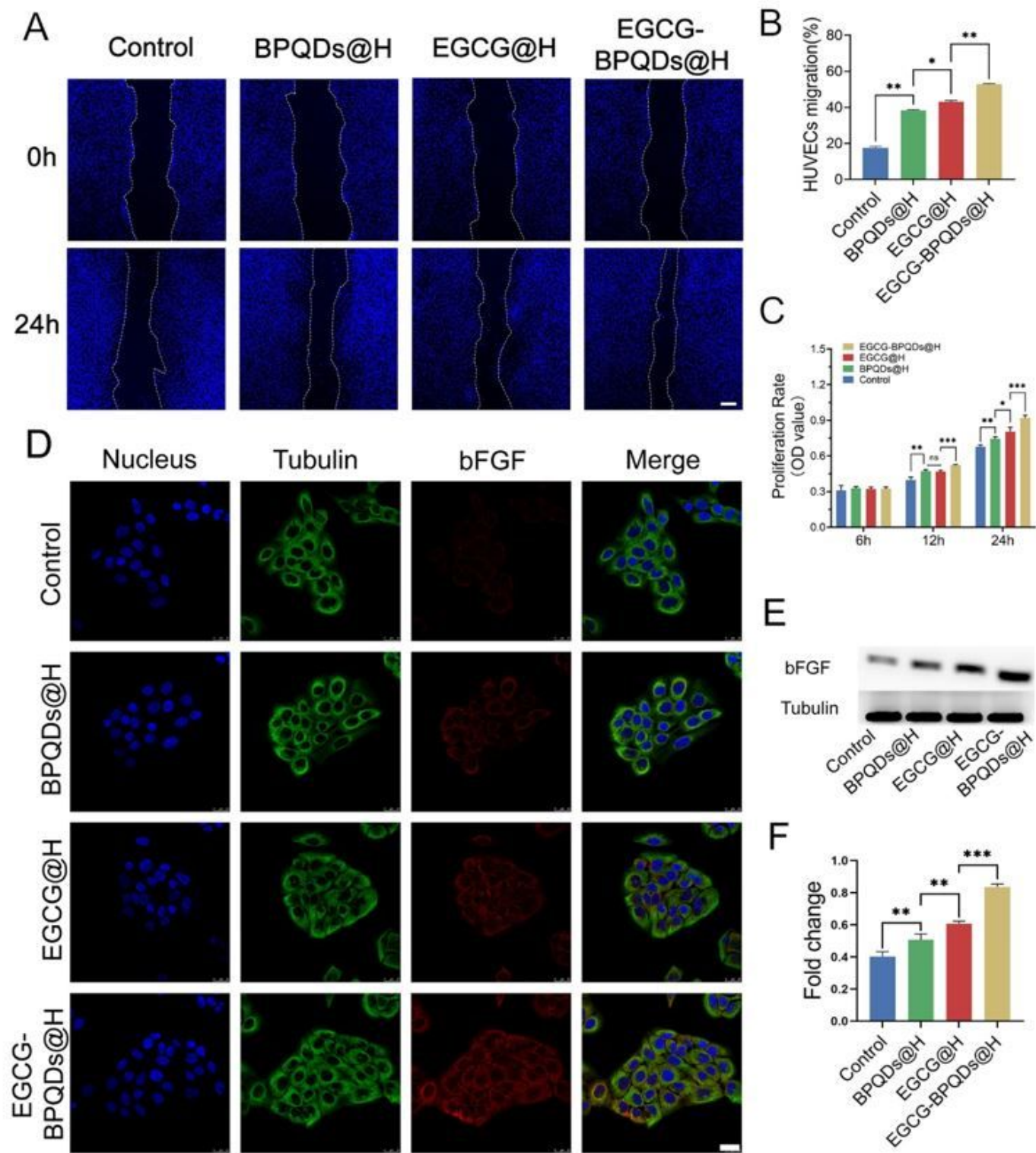


Figure 5

Promoting migration and proliferation effects and potential mechanism. (A) Digital images of scratch wound assay in different treatments, bar=100µm. (B) Quantification of HUVEC migration. (C) MTT analysis in different groups. (D) CLSM images of the expression analysis of bFGF, bar=25µm. (E) The expression level of bFGF protein. (F) Quantification analysis of the bFGF protein. *P< 0.05, **P< 0.01, ***P< 0.001.

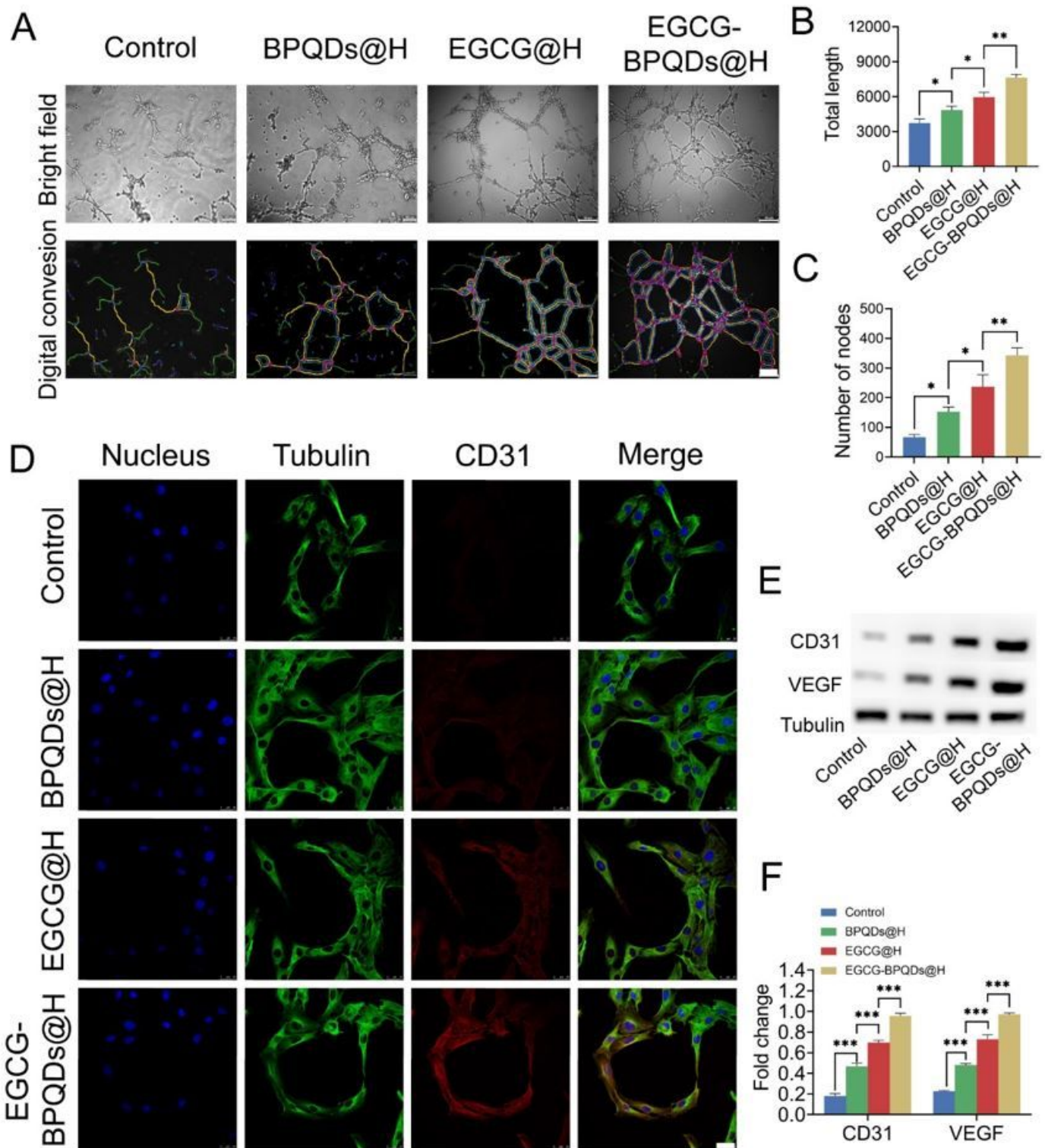


Figure 6

Angiogenic tubular formation and relative protein expression of endothelial cells in vitro. (A) Tubular formation on Matrigel and digital analysis conversion of HUVECs in different treatments, bar=100µm. (B, C) Total of length and the number of nodes were quantified. (D) CLSM images of the expression analysis of CD31, bar=25µm. (E) The expression level of CD31 and VEGF protein. (F) Quantification analysis of the CD31 and VEGF protein. *P< 0.05, **P< 0.01, ***P< 0.001.

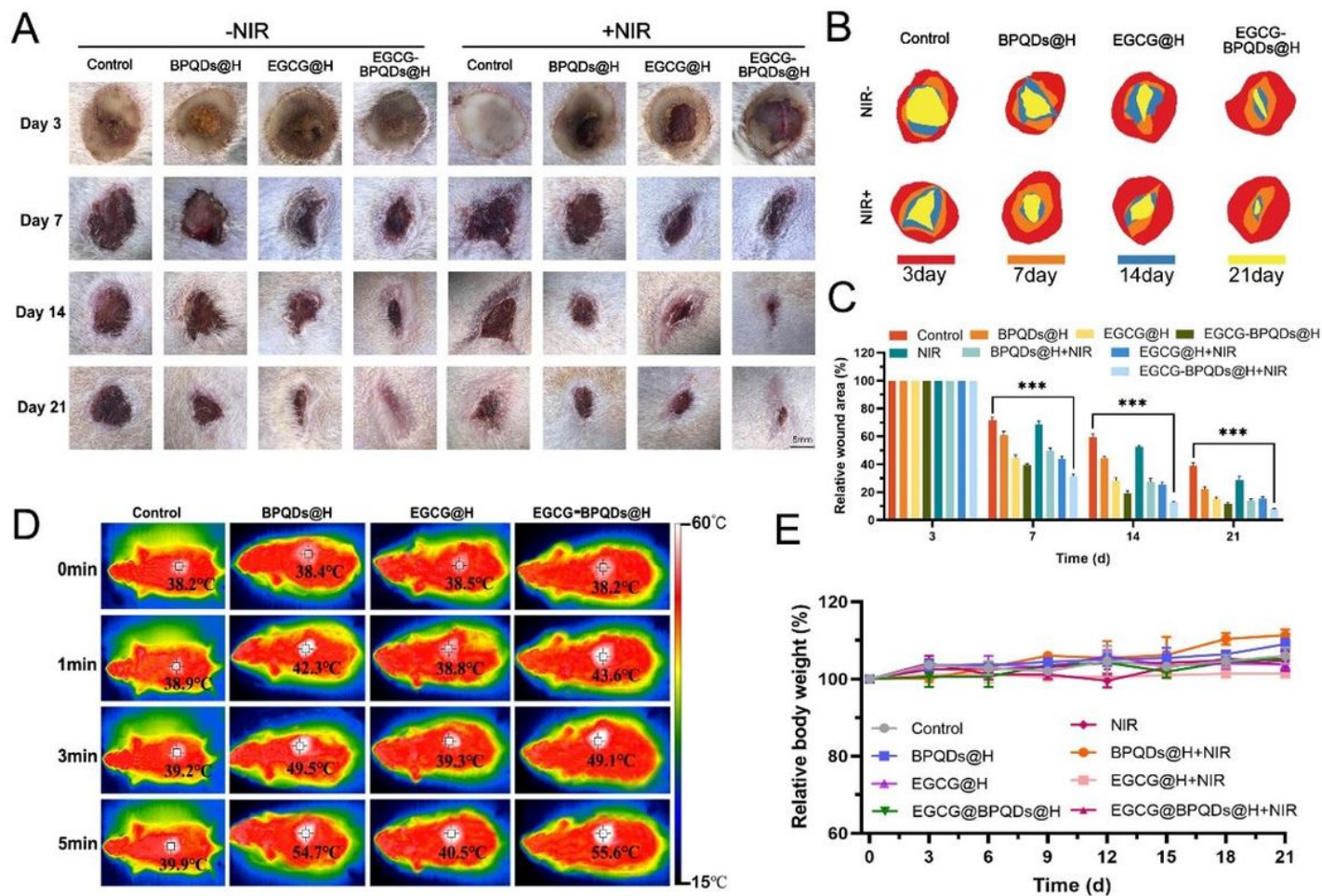


Figure 7

Evaluation effects of accelerating diabetic infected burn-wound in vivo. (A) Images of infected burn-wound healing at different times, bar=5mm. (B) Traces of wound-bed closure during 21 days for each treatment. (C) Corresponding statistical graph of relative wound area from each group with different treatments. (D) Photothermal images of rats treated with hydrogel, BPQDs@H, EGCG@H and EGCG-BPQDs@H with NIR irradiation at different times. (E) Changes of body weight of the rats.

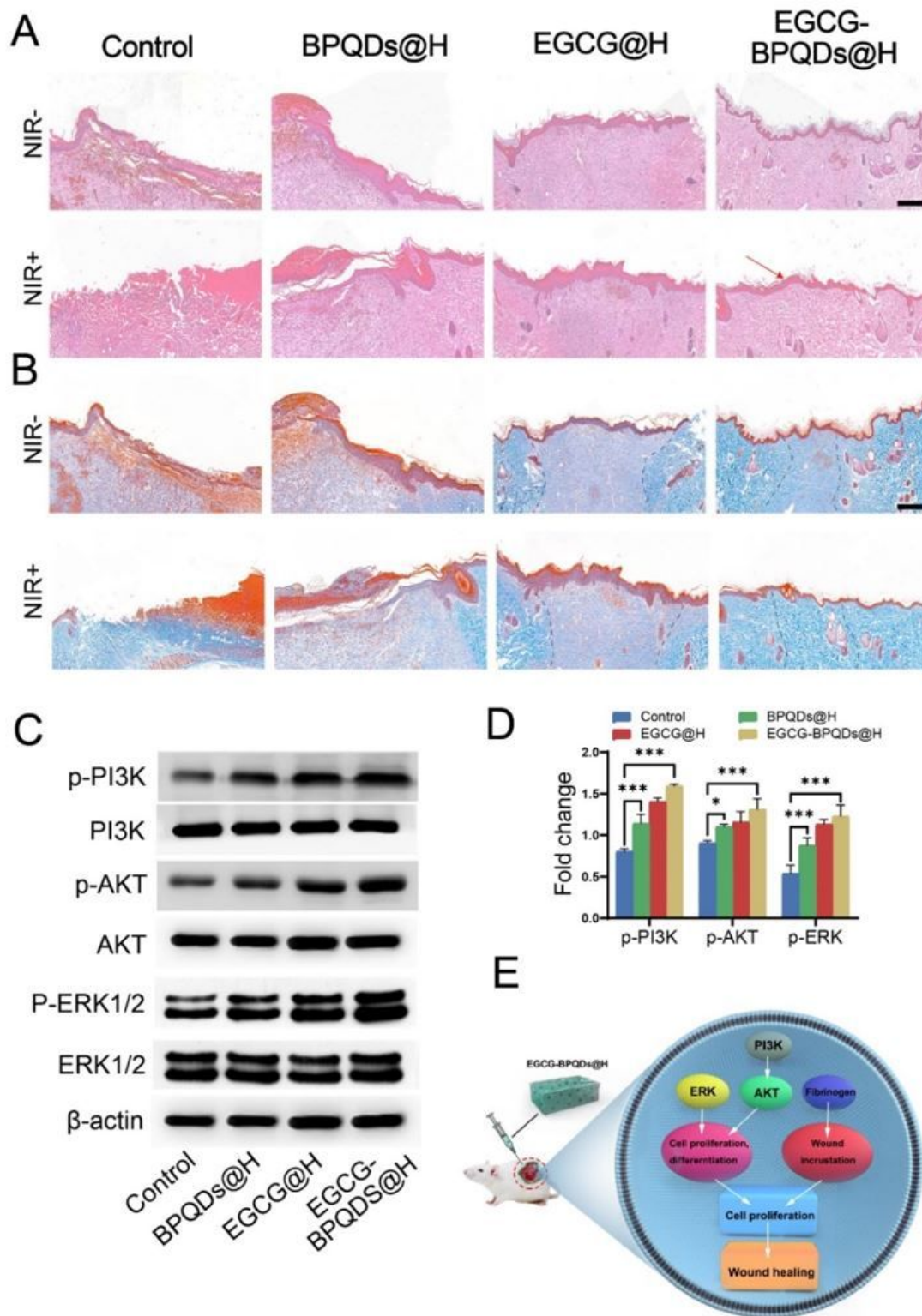
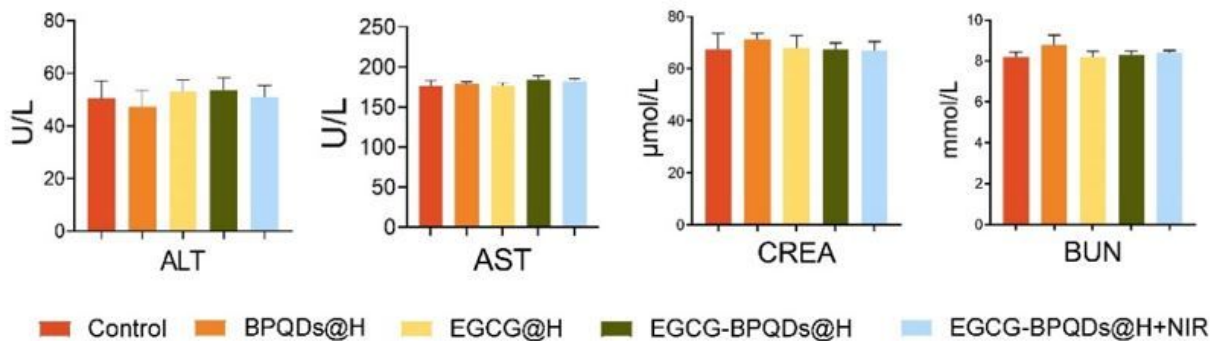


Figure 8

Evaluation on the healing-promoting effect of the nanoplatform on infected burns rats. (A) H&E staining of wound sites with different treatments, red arrow indicates intact epidermis, bar=200 μ m. (B) Masson staining of the wound tissues, dotted line indicates collagen at the wound, bar=200 μ m. (C) Western blot analysis. (D) Quantification for the molecules involved in the signaling pathways for burn wound healing.

(E) Scheme diagram showing nanomaterials direct cell proliferation, and enhanced fibrinogen expression to accelerate the wound healing.

A



B

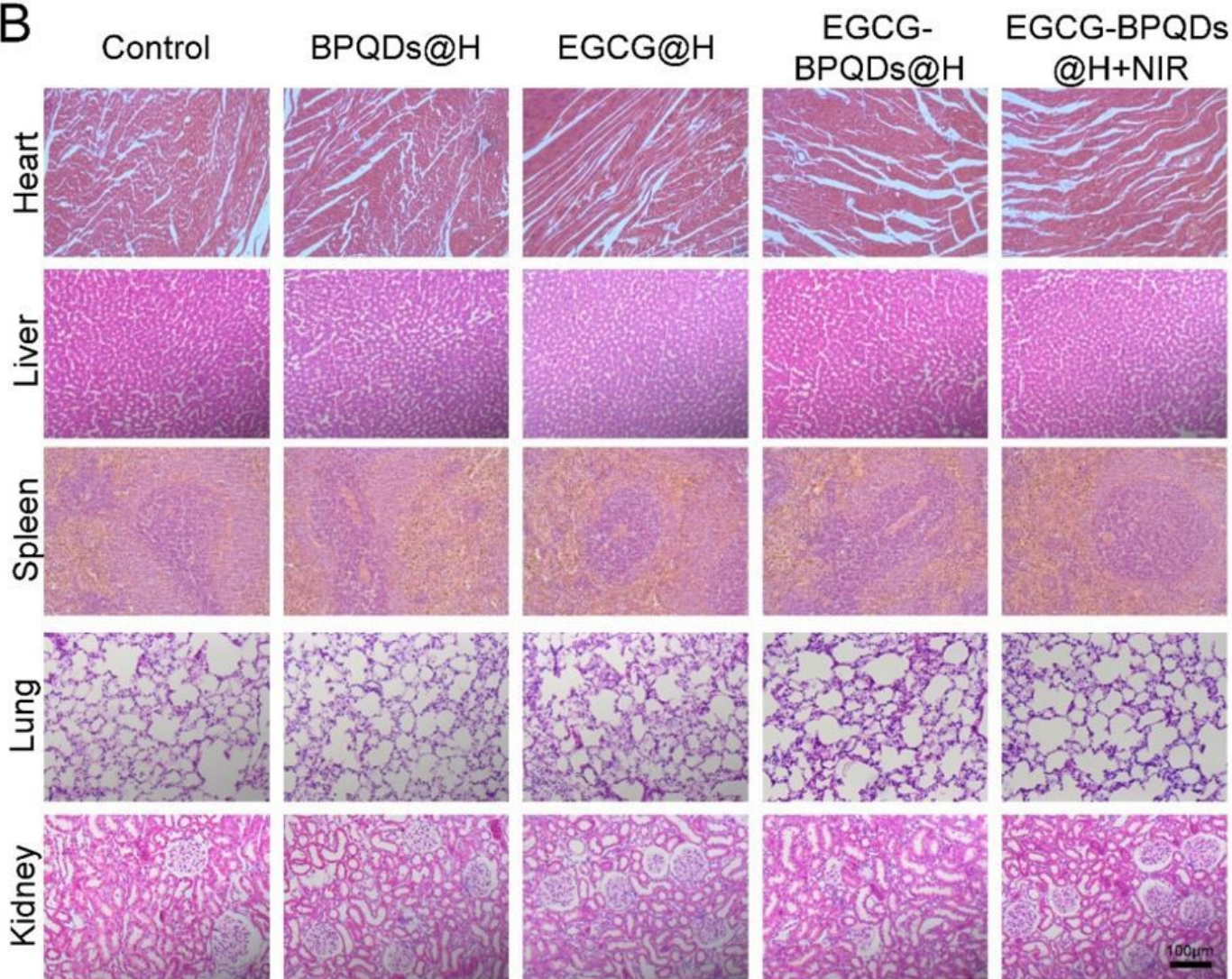


Figure 9

Preliminary toxicity study in vivo. (A) Hepatorenal function test for ALT, AST, CREA and BUN. (B) Histological toxicological observation of H&E staining of the heart, liver, spleen, lung and kidney with different treatments, bar=100 μm .

Supplementary Files

This is a list of supplementary files associated with this preprint. Click to download.

- [GraphicAbstract.docx](#)
- [SupportingInformation.docx](#)
- [scheme1.jpg](#)